Highlights

Lane-keeping control of automated vehicles with feedback delay: nonlinear analysis and laboratory experiments

Illés Vörös,Dénes Takács

- Linear and nonlinear analyses of a single-track vehicle model with linear feedback control for lane-keeping

- Subcritical Hopf bifurcations and low amplitude unstable limit cycles are detected around the stable equilibrium

- Safe and unsafe zones of stabilizing control gains are specified, based on limit cycle amplitudes

- The safe and unsafe control gain zones are also identified in a series of small-scale laboratory experiments on a conveyor belt

Lane-keeping control of automated vehicles with feedback delay: nonlinear analysis and laboratory experiments

Illés Vörös[a,*], Dénes Takács[b]

[a]MTA-BME Research Group on Dynamics of Machines and Vehicles, Műegyetem rkp 5, Budapest 1111, Hungary
[b]Department of Applied Mechanics, Budapest University of Technology and Economics, Műegyetem rkp 5, Budapest 1111, Hungary

ARTICLE INFO

ABSTRACT

The feedback control of automated lane-keeping of passenger cars is analyzed in this paper. The calculations are based on the single-track vehicle model with the consideration of steering system dynamics. A linear feedback controller is used to control the lateral dynamics, while taking into account feedback delay and the effects of the lower-level steering controller. Subcritical Hopf bifurcations are detected along the linear stability limits and the emerging branches of periodic orbits are followed using numerical continuation. It is shown that low amplitude unstable limit cycles exist around the stable equilibrium of straight-line motion for certain parameter ranges. Based on the limit cycle amplitudes, safe and unsafe zones of stabilizing control gains are specified. The unsafe control gain zones within the linearly stable domain are also identified under laboratory conditions using small-scale experiments on a conveyor belt. The theoretical and the practical results show good accordance with respect to the domain of attraction of the straight-line motion.

1. Introduction

Unintended lane departures have been identified as one of the most common causes of passenger car road accidents [9, 23]. The related advanced driver assistance systems and autonomous driving functions, such as lane-keeping and lane changing control have the potential to reduce the severity, or even completely avoid a large number of such accidents [39, 31]. The effectiveness of these driving functions depends on the performance of the steering control system used in the vehicle.

Because of this huge potential with regards to traffic safety, the control of the lateral dynamics of the vehicle has been extensively researched in the last few decades [33, 1]. Traditionally, the reliable methods of linear system theory are used to design and develop these controllers. Solutions have been proposed based on most classical methods, including proportional-integral-derivative [50] and optimal control techniques [30], as well as robust $\mathcal{H}_\infty$ [5] and adaptive methods [51]. The pure pursuit [2] and Stanley [18] controllers are also very widely used solutions to the path following problem, thanks to their simple geometric considerations without the need for a more involved vehicle model. Nonlinear control methods have also been successfully applied to the trajectory tracking problem, including feedback linearization [25, 48] and utilizing flatness properties [13] in the case of certain vehicle models. Additional nonlinear approaches include Lyapunov-based control design [36] and sliding mode controllers [35, 41], and with the advances in optimization techniques and computational resources, nonlinear model predictive control is also becoming a viable option [14].

These more sophisticated design techniques can often inherently lead to better performing and more robust con-

trollers. However, two important classes of phenomena that are often only indirectly considered or approximated in the design process are robustness against nonlinearities and time delay. It has been shown that both of these aspects have a non-negligible effect on the dynamics of the controlled vehicle: the presence of time delay (which may include effects such as sensor delay, processing time and actuator dynamics) greatly reduces the size of stable parameter domains, which can lead to undesirable oscillations and even stability loss [17, 46, 19]. Nonlinearities, on the other hand, may lead to the presence of unstable limit cycles around stable equilibria, which means that certain perturbations (which might stem from e.g. road surface irregularities, wind gusts or sensor noise) can cause instability even if the system is stable in the linear sense [6, 27, 43, 44, 32]. The most common sources of nonlinearities in vehicle motion control include tire force saturation and geometrical nonlinearities. Because of its safety implications, the nonlinear dynamics of passenger cars have already been widely researched, but the focus has mostly been on the cornering behavior of the uncontrolled vehicle [8, 37] or on the presence of a human driver [6, 27, 26, 29].

The modeling of the human driver is in fact often approached from a control theory viewpoint (see [28] and [34] for examples of human driver models with varying complexity) and a large number of significant results have already been published with regards to the nonlinear dynamics of the vehicle driver interaction. The local dynamics near a Hopf bifurcation point can be analyzed with the help of normal form calculation. This has been performed in [19] for a four-wheel-steering vehicle model with the consideration of the driver's reaction time delay. A higher-order nonlinear analysis was presented in [26], but the time delay of the driver was approximated as a first-order system. Bifurcation diagrams were constructed in [27] using a large number of numerical simulations where the driver's action was perturbed by

a periodic forcing function. As a result, quasi-periodic and chaotic solutions have been uncovered. The large computational demand of constructing bifurcation diagrams based on numerical simulations can be avoided by using continuation methods to follow branches of periodic solutions along a system parameter. This has been performed in [6, 7] and [29], thereby uncovering the nonlinear dynamics of the system farther away from the bifurcation points. Unsafe zones inside the linearly stable parameter domains have already been identified in [6] and [7], but with a focus on different parameters and with different modeling considerations than here. In [29], the nonlinear behavior of a 14 degrees-of-freedom multibody vehicle model was also analyzed by simulation studies, and the results were verified in a human controlled driving simulator.

In this paper, we present an extended analysis and experimental validation of the subcritical behavior of a lane keeping controller reported in [44]. The main contribution of the present work compared to most related research in the literature is threefold: while in the majority of the cases [6, 19, 26, 27, 29, 32, 8, 37], the standard bicycle model is used with a nonlinear tire side force characteristic, our vehicle model includes the dynamics and saturation of the steering mechanism, the geometrical nonlinearities and the tire self-aligning moments. We show that this modeling choice greatly affects the results. Secondly, the time delay in the system is considered explicitly in our work, instead of approximating it by a first order lag term (as in e.g. [6, 26, 29]). Finally, we use numerical continuation methods [24, 40, 11, 42] on the resulting time delay system to highlight unstable limit cycles (unstable periodic orbits/solutions) that indicate sensitivity to initial conditions and perturbations in certain, linearly stable parameter ranges. The resulting bifurcation diagrams allow the designer to know what kinds of behaviors to expect due to large disturbances in different parameter ranges, which is crucial for reliable and safe control design.

Although only a simple, delayed feedback controller is considered in this paper, this allows us to gain a deeper understanding of the controlled system. In particular, the low number of control parameters makes it possible to thoroughly analyze a large domain of stabilizing control gains by performing numerical bifurcation analysis. Additionally, the control parameters have a clear physical meaning, therefore the resulting bifurcation diagrams are easier to understand and more fundamental conclusions can be drawn, that can be considered during the design of more complex control systems. The proposed approaches can be used to gain a deeper understanding of the potential dynamics and verify the robustness of other control methods too. The presented techniques can also be used as a basis of comparison between different controllers.

The sensitivity of the lane-keeping controller to perturbations in certain parameter ranges that our theoretical calculations suggest has been successfully reproduced in a series of laboratory experiments using a small-scale test rig originally proposed in [45]. This novel experimental setup consists of an RC car anchored to the frame of a conveyor

belt using a special fixture that constrains only the longitudinal displacement of the car. The conveyor belt provides the longitudinal speed of the vehicle, while the steering angle of the car can be adjusted using a real-time control system.

This provides a suitable environment for fast hardware-in-the-loop testing of various steering control methods under laboratory conditions, before performing full-scale, real vehicle test drives, as in e.g. [10, 49]. The experimental comparison of several classical lateral control laws is included in [10], while the real vehicle tests in [49] focus on nonlinear Lyapunov-based controllers. In terms of laboratory testing of autonomous driving functions, an elaborate approach was presented in [15], where the vehicle itself is mounted on a roller test bench and only the relative movement of other traffic participants is realized using wheeled mobile robots. Overall, laboratory tests provide a more cost effective, fast and repeatable way of control system verification, potentially allowing faster design iterations before the eventual real vehicle test drives are performed. Using the small-scale experimental setup, an extensive series of measurements were carried out to uncover the sensitivity of the closed loop system to perturbations along the linearly stable domain of control gains. The results of this unique and comprehensive experimental nonlinear analysis show very good qualitative and quantitative agreement with the theoretical calculations in terms of safe and unsafe zones of control gains within the linearly stable region, which can be used as a guideline when tuning the controller.

The rest of the paper is organized as follows: the vehicle model with the lane-keeping controller is presented in Section 2.1, with a subsequent analysis in terms of both linear and nonlinear behavior in Sections 2.3 and 2.4, respectively. The results presented in Section 2 are calculated using the parameter values of a real passenger car. The experimental setup is presented in Section 3.1, while the mechanical model is modified in Section 3.2 to better represent the dynamics of the vehicle on the test rig. The differences between the original and the modified vehicle model are analyzed in Section 3.3. Section 3.4 is devoted to the experimental results and our analysis is concluded in Section 4.
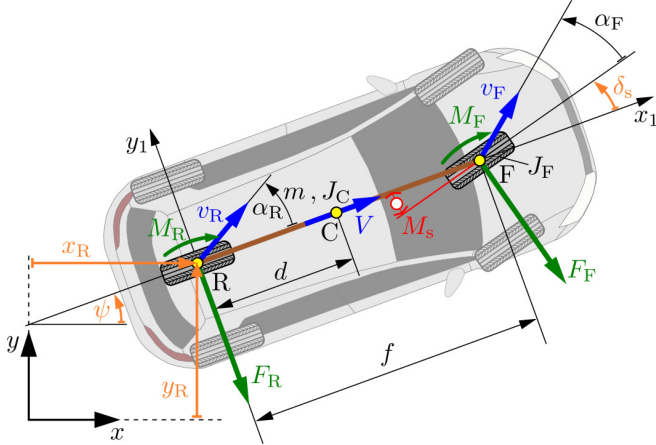
2. Single track vehicle model with lane-keeping control

In this section, an extended single track vehicle model is presented, which includes the dynamics of the steering system, similarly to [3]. The resulting vehicle model is equipped with a linear feedback controller for lane keeping, and the closed-loop system is analyzed in terms of linear and nonlinear dynamics. This section is intended to represent a real passenger car (as opposed to the experimental setup in Secion 3) both in terms of mechanical model and parameter values.

2.1. Mechanical modeling

The single track model of cars, also called in-plane bicycle model, is the most commonly used mechanical model to

represent the lateral dynamics of a vehicle. Its main assumption is that the tire contact patches are summarized along each axle into a substitutive contact patch located at the longitudinal axis of the symmetric vehicle. In addition, the height of the center of gravity is assumed to be zero, therefore, neither the pitching nor the rolling of the vehicle are considered.

Figure 1: The single-track vehicle model with steering dynamics.

The vehicle model is shown in Fig. 1. We use the global coordinates x_R and y_R of the rear axle (point R), the heading angle ψ and the steering angle δ_s as generalized coordinates. The vehicle parameters include the mass m, yaw moment of inertia J_C about the center of mass (point C), and the geometrical parameters f (wheelbase) and d as defined in Fig. 1. The dynamics of the steering actuation are considered using the mass moment of inertia J_F of the steering system. Assuming a constant longitudinal speed V (which models a rear wheel drive vehicle), the following kinematic constraint can be defined:

$$\dot{x}_R \cos \psi + \dot{y}_R \sin \psi = V \,. \tag{1}$$

The presence of this kinematic constraint makes the system non-holonomic. There is a number of methods available to derive the equations of motion of such systems [21, 4]. Here, we use the Gibbs–Appell-method [16], since it leads to the most compact, first order form of the equations, with the minimum number of coordinates. This approach requires the definition of so-called pseudo velocities. Since four generalized coordinates and one kinematic constraint govern the system, three appropriately chosen pseudo velocities can describe the velocity state. Let us define these as the lateral velocity σ_1 of point R, the vehicle yaw rate σ_2 and the steering rate σ_3. Using the definitions of the pseudo velocities and the kinematic constraint (1), the time derivatives of the generalized coordinates can be expressed as

$$\dot{x}_R = V \cos \psi - \sigma_1 \sin \psi \,, \tag{2}$$
$$\dot{y}_R = V \sin \psi + \sigma_1 \cos \psi \,, \tag{3}$$
$$\dot{\psi} = \sigma_2 \,, \tag{4}$$

$$\dot{\delta}_s = \sigma_3 \,. \tag{5}$$

The rest of the dynamics are described by the Gibbs–Appell-equations (see the Appendix for the details of the derivation):

$$\begin{bmatrix} m & md & 0 \\ md & J_C + md^2 + J_F & J_F \\ 0 & J_F & J_F \end{bmatrix} \begin{bmatrix} \dot{\sigma}_1 \\ \dot{\sigma}_2 \\ \dot{\sigma}_3 \end{bmatrix} = \begin{bmatrix} f_1 \\ f_2 \\ f_3 \end{bmatrix}, \tag{6}$$

where the right-hand side consists of

$$f_1 = -F_R - F_F \cos \delta_s - mV \sigma_2 \,, \tag{7}$$
$$f_2 = -M_F - M_R - F_F f \cos \delta_s - mdV \sigma_2 \,, \tag{8}$$
$$f_3 = -M_F + M_s \,. \tag{9}$$

M_s denotes the steering torque acting as an internal torque between the vehicle body and the front wheel. $F_F(\alpha_F)$ and $F_R(\alpha_R)$ are the lateral tire forces, while $M_F(\alpha_F)$ and $M_R(\alpha_R)$ are the self-aligning moments (see Fig. 1). Subscripts F and R refer to the front and rear wheels, respectively. The tire force and moment characteristics are described by the nonlinear brush tire model (see Fig. 2 and Appendix A for details) as a function of the side slip angles

$$\alpha_F = \arctan \left(\frac{(\sigma_1 + f \sigma_2) \cos \delta_s - V \sin \delta_s}{(\sigma_1 + f \sigma_2) \sin \delta_s + V \cos \delta_s} \right), \tag{10}$$

$$\alpha_R = \arctan \left(\frac{\sigma_1}{V} \right) \,. \tag{11}$$

It is worth noting that including the tire self-aligning moments has a strong effect on the dynamics of the steering system (see Eq. (9)), therefore, their inclusion in the vehicle model is essential.
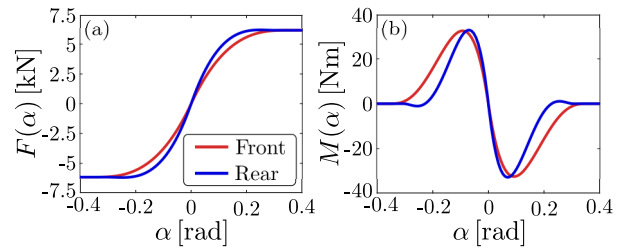
Figure 2: Lateral tire force and self-aligning moment characteristics of the brush tire model with parameters listed in Table 2.

2.2. Hierarchical lane-keeping control

Without loss of generality, we define our control goal as stabilizing straight-line motion along the x-axis. To achieve this, the desired steering angle is generated by feeding back the lateral position y_R and the yaw angle ψ of the vehicle using the proportional gains P_y and P_ψ:

$$\delta_s^{\text{des}}(t) = -P_y y_R(t - \tau) - P_\psi \psi(t - \tau) \,. \tag{12}$$

In the above control law, the feedback delay τ represents the total time delay in the system, consisting of sensor delays, sampling times, data processing and communication,

etc. Note that feeding back the lateral position and yaw angle as in Eq. (12) can be considered as a linearized version of a basic preview model [47], where the predicted vehicle position $y_R(t+T)$ is used as feedback using the preview time T. In case of straight-line trajectory: $\delta_s^{des}(t) = -P_y y_R(t+T) \approx -P_y y_R(t) - P_y V T \psi(t)$. Therefore, considering $P_y V T = P_\psi$, some preview effect is inherently considered in the gain P_ψ, which is beneficial for compensating the feedback delay τ.

In order to realize the desired steering angle δ_s^{des}, the steering torque M_s is generated according to the lower-level PD controller

$$M_s = -k_p \left(\delta_s - \text{sat} \left(\delta_s^{des} \right) \right) - k_d \sigma_3, \tag{13}$$

with proportional and derivative gains k_p and k_d. In order to prevent unreasonably large steering angles, a saturation function sat is used to limit δ_s^{des} to the range of $-30°$ to $30°$ (see Appendix B for details). For the sake of simplicity, the desired steering rate is kept at zero, therefore the derivative gain k_d multiplies only σ_3 in Eq. (13) and it is assumed that the time delay of the lower-level controller can be neglected compared to τ in Eq. (12).

2.3. Linear stability analysis

The desired steady state of straight-line motion along the x-axis corresponds to the generalized coordinate and pseudo-velocity values

$$\begin{aligned} x_R(t) = Vt, \; y_R(t) \equiv 0, \; \psi(t) \equiv 0, \; \delta_s(t) \equiv 0, \\ \sigma_1(t) \equiv 0, \; \sigma_2(t) \equiv 0, \; \sigma_3(t) \equiv 0. \end{aligned} \tag{14}$$

Since only the coordinates y_R and ψ are used in the control law in Eq. (12), the vehicle's position in the x direction will have no influence on the dynamics and the corresponding Eq. (2) can be decoupled from the rest of the equations of motion. The rest of the state variables can be collected into the state vector

$$\mathbf{x} = \begin{bmatrix} y_R & \psi & \delta_s & \sigma_1 & \sigma_2 & \sigma_3 \end{bmatrix}^T, \tag{15}$$

where the steady state in Eq. (14) corresponds to $\mathbf{x}(t) \equiv \mathbf{0}$. For small oscillations around this equilibrium, the linearized system can be written as $\dot{\mathbf{x}} = \mathbf{Ax} + \mathbf{B}u$, with $u = \delta_s^{des}$ as the control input, and the state and input matrices

$$\mathbf{A} = \begin{bmatrix} 0 & V & 0 & 1 & 0 & 0 \\ 0 & 0 & 0 & 0 & 1 & 0 \\ 0 & 0 & 0 & 0 & 0 & 1 \\ 0 & 0 & A_{43} & A_{44} & A_{45} & A_{46} \\ 0 & 0 & A_{53} & A_{54} & A_{55} & A_{56} \\ 0 & 0 & A_{63} & A_{64} & A_{65} & A_{66} \end{bmatrix}, \tag{16}$$

$$\mathbf{B} = -\frac{k_p}{k_d} \begin{bmatrix} 0 & 0 & 0 & A_{46} & A_{56} & A_{66} \end{bmatrix}^T, \tag{17}$$

where the matrix elements A_{ij} are listed in Appendix C.1. If the proportional gains P_y and P_ψ are collected into the gain vector

$$\mathbf{K} = \begin{bmatrix} -P_y & -P_\psi & 0 & 0 & 0 & 0 \end{bmatrix}, \tag{18}$$

then the linear control law in Eq. (12) can be written as $\delta_s^{des}(t) = \mathbf{Kx}(t-\tau)$. Note that from the point of view of designing the upper-level control law in Eq. (12), the lower-level controller (13) can be considered as part of the system dynamics, i.e. it is included in matrices $\mathbf{A}$ and $\mathbf{B}$.

The bicycle model with the corresponding lane-keeping controller can be written in the linear delay differential equation form $\dot{\mathbf{x}}(t) = \mathbf{Ax}(t) + \mathbf{BKx}(t-\tau)$. Using an exponential trial function, the characteristic equation of this system is of the form

$$D(\lambda) := \det \left(\lambda \mathbf{I} - \mathbf{A} - \mathbf{BK}e^{-\lambda\tau} \right) = 0, \tag{19}$$

where $\lambda \in \mathbb{C}$ denotes the characteristic exponent and $\mathbf{I}$ is the identity matrix. At the boundaries of stability, there exist characteristic exponents that lie on the imaginary axis of the complex plane, i.e. $\lambda = \pm i\omega$. If $\omega = 0$, a real characteristic exponent may cross the imaginary axis and a static loss of stability occurs. This happens if $D(0) = 0$, leading to:

$$P_y k_p \frac{C_F(f C_R - \tilde{C}_R) + C_R \tilde{C}_F}{m J_F J_C} = 0, \tag{20}$$

i.e. the control gains $P_y = 0$ and $k_p = 0$ correspond to the boundaries of static loss of stability. Parameters C_F, C_R, $\tilde{C}_F$ and $\tilde{C}_R$ in Eq. (20) are the parameters of the linearized tire characteristics, as defined in Appendix A. It can be seen that for certain vehicle configurations, the numerator of Eq. (20) can be zero regardless of the control gains, but in this paper, we are only focusing on the effects of the controller and use vehicle parameters for which this problem does not occur.

In case of $\omega > 0$, a complex conjugate pair of characteristic exponents may move to the right half plane, and the system loses its stability by oscillating with the angular frequency ω. Substituting $\lambda = i\omega$ into Eq. (19), the equation $D(i\omega) = 0$ can be separated into its real and imaginary parts. These two equations can then be solved for two arbitrary system parameters, resulting in the parametric curves of dynamic stability loss (the so-called D-curves, parametrized by ω) in the plane of these two system parameters.

Performing the above calculations, the stable domains of the control gains P_y and P_ψ can be generated according to Fig. 3. The stability charts are plotted for realistic vehicle parameter values listed in Tables 1 and 2, following [44]. As nominal values, we use a vehicle speed of 80 km/h and a time delay of 0.25 s, both of which are moderate values in case of a real passenger car. Panels (a) and (b) show that further increasing the value of these two parameters greatly reduces the stable domains. This is less of a problem in case of the vehicle speed, since it can be measured rather accurately, but neglecting the time delay in the system can lead to a severe overestimation of the stable domain. Increasing the lower level control gains k_p and k_d (panels (c) and (d)) also reduces the range of stabilizing P_y and P_ψ values. In the limit, if k_p tends to infinity, the lower-level controller completely overcomes the dynamics of the steering system, and the resulting stable domain converges to the stability map of a simpler vehicle model, where the steering angle is directly

Table 1
Parameter values of a passenger car.

Parameter	Value
Vehicle wheelbase (f)	2.7 m
Distance between rear axle and center of gravity (d)	1.35 m
Vehicle mass (m)	1430 kg
Yaw moment of inertia (J_C)	2500 kgm^2
Steering system moment of inertia (J_F)	0.25 kgm^2
Lower-level steering control proportional gain (k_p)	640 Nm
Lower-level derivative gain (k_d)	8 Nms
Longitudinal velocity (V)	80 km/h
Time delay (τ)	0.25 s

Table 2
Tire parameters of a passenger car.

Parameter	Front axle	Rear axle
Contact patch half-length (a)	0.05 m	0.05 m
Cornering stiffness (C)	50 kN	67 kN
Sliding friction coefficient (μ)	0.88	0.88
Rolling friction coefficient (μ_0)	0.88	1
Vertical axle load (F_z)	7014 N	7014 N

assigned as the system input. The stability boundary of this simpler model is plotted in dotted line in Fig. 3(c); for details, the reader is referred to [44].

2.4. Nonlinear analysis

The boundaries of dynamic loss of stability determined in Section 2.3 correspond to Hopf bifurcations in the nonlinear system [24, 40]. This means that limit cycles exist in the state space for certain parameter ranges, leading to intricate system dynamics that also depend on the initial conditions. If the Hopf bifurcation is subcritical, the domain of attraction of the stable straight-line motion can be bounded by an unstable limit cycle. This means that if the system is sufficiently perturbed, the domain of attraction of the stable equilibrium is left, and the motion of the vehicle diverges from the reference path even though the linear stability maps

Figure 3: Stability charts of the control gains P_y and P_ψ for various values of (a) vehicle speed V, (b) time delay τ, (c) lower-level proportional gain k_p and (d) lower-level derivative gain k_d. The largest stable area is shaded in gray in each panel. Dashed curves correspond to the nominal parameter values listed in Table 1, while the dotted line in panel (c) refers to the stability boundary of the bicycle model with directly assigned steering angle.
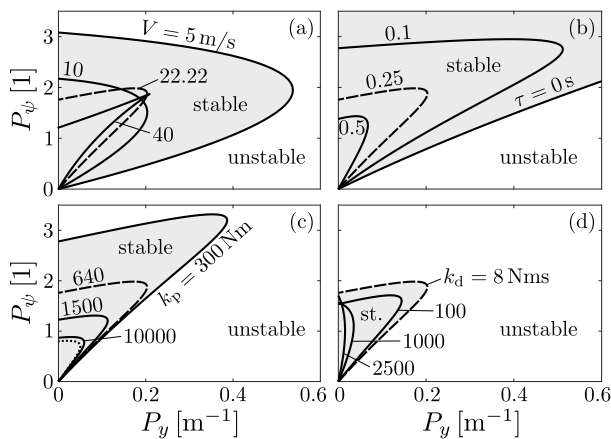
suggested otherwise.

In order to uncover these unstable limit cycles and map out the domains of attraction, we use numerical continuation with the help of the Matlab package DDE-Biftool [11, 12, 38]. The limit cycle is calculated using orthogonal collocation near the Hopf bifurcation point and it is followed along a system parameter by the pseudo-arclength method to form a branch of limit cycles in the bifurcation diagram of the system. To avoid computational challenges, the saturation of the control input in Eq. (13) is smoothed out using second-order polynomials (see Appendix B), which is a common technique in case of non-smooth systems (see, for example, [22]).
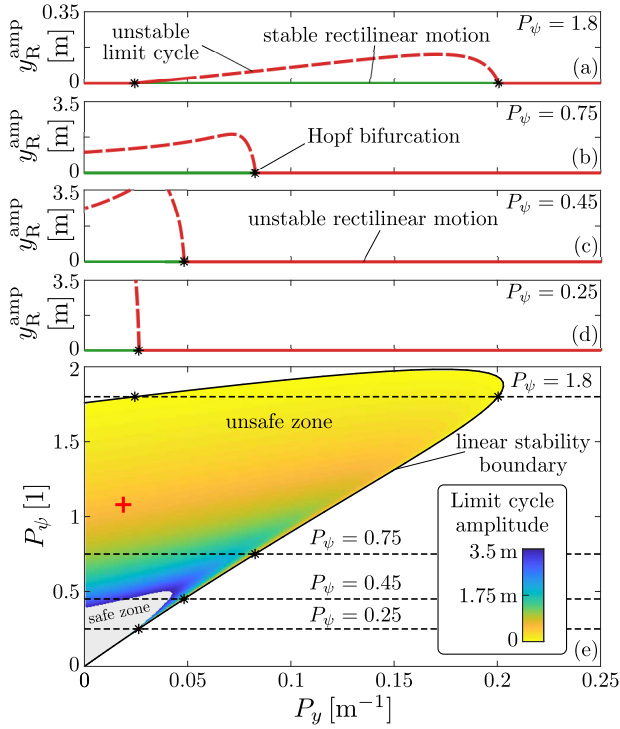
The amplitudes of the detected limit cycles are used to quantify the domain of attraction of the straight-line motion. In particular, the amplitude y_R^{amp} of the lateral position is plotted in the bifurcation diagrams of this study. This, however, does not coincide with the maximum disturbances for which the vehicle tends back to the straight-line motion, i.e. this is not the exact boundary of the domain of attraction, since that depends on the rest of the state variables too. Moreover, due to the feedback delay in the controller, the phase space of the system is in fact infinite dimensional, therefore we can only show certain sections of the phase space. Nevertheless, the resulting bifurcation diagrams are still good indicators of the sensitivity of different parameter regions to initial conditions and disturbances.

In order to verify the results of numerical continuation and to detect possible disconnected branches of limit cycles, a comprehensive series of numerical simulations was performed along the amplitude and control gain regions depicted in the bifurcation diagrams. Although a large number of initial conditions in terms of y_R was used for the simulations, the infinite dimensional phase space makes it very hard to thoroughly verify the (non-)existence of additional solutions. Nevertheless, the simulations confirmed the limit cycles uncovered using numerical continuation, while no additional solutions were found in the region depicted in the bifurcation diagrams.

Figure 4 shows the results of the nonlinear analysis for the vehicle parameters in Tables 1 and 2. For the investigated setup, the linear stability boundary of dynamic stability loss corresponds to subcritical Hopf bifurcations, which means that unstable limit cycles are present in the phase space of the nonlinear system. Panels (a)-(d) show bifurcation dia-

Figure 4: Bifurcation analysis of the controlled vehicle. Panels (a)-(d) show individual bifurcation diagrams for different sections of the stability chart, while the coloring in panel (e) refers to the amplitudes y_R^{amp} of the unstable limit cycles in the linearly stable control gain domain. Red plus sign denotes the optimal gain setup of the linear closed-loop system.

grams using the control gain P_y as bifurcation parameter for different fixed values of the control gain P_ψ. Solid green and solid red horizontal lines at $y_R^{amp} = 0$ m correspond to linearly stable and unstable straight-line motions, respectively, and are separated by the Hopf bifurcation points marked by black stars. The branches of unstable limit cycles are denoted by dashed red curves. Based on the bifurcation diagram, the linear stability chart is extended in panel (e) with a colormap that indicates the amplitude of the unstable limit cycles in the linearly stable domain of control gains. In the bright yellow range, the system can leave the domain of attraction of straight-line motion even for small perturbations, while in the dark blue range much larger perturbations are required to do this. As the coloring shows, although the system is stable in the linear sense, the domain of attraction can become dangerously small, especially for larger values of the control gain P_ψ (cf. panels (a)-(d) and the corresponding horizontal dashed lines in panel (e)). Hence, we call this region of the linearly stable domain of the control gains unsafe zone.

We have also calculated the optimal control gain setup based on traditional linear design (denoted by a red plus sign in panel (e)), where the rightmost characteristic exponent of the linear closed-loop system has the smallest (negative) real part, i.e. the system has the largest damping. This optimal setup ensures the fastest decay of the vibrations in the lin-

ear domain, but the domain of attraction of the straight-line motion is relatively small and the closed-loop system is vulnerable to disturbances.

In the gray parameter range of panel (e), the amplitude of the limit cycles exceeds 3.5 meters (the width of a single lane on a normal road). We refer to this region as a safe zone, where, without leaving the domain of attraction of the desired straight-line motion, one can accomplish a lane change manoeuvre simply by changing the controller's reference signal to the center line of the adjacent target lane. In addition, the amplitude of the limit cycles in this gray area start to increase very strongly, leading to physically less relevant results.

As shown in Fig. 4, the domain of attraction of the straight-line motion is strongly limited in a major part of the linearly stable control gain domain. Without the detailed nonlinear analysis of the system, one could introduce a significant safety hazard into the motion control of the vehicle by choosing the control gains based on the linear stability analysis only. In the next section, the existence of this safety issue is demonstrated in laboratory experiments.

3. Small-scale experimental setup

3.1. Test rig
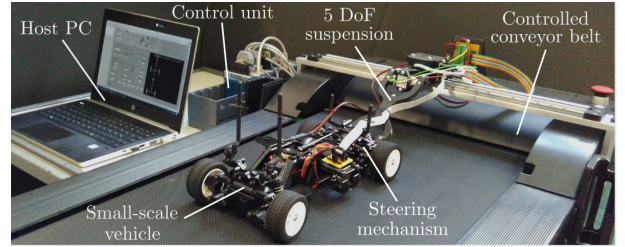
Figure 5: The experimental setup.

The experiments were performed on a small-scale test environment that was originally proposed and presented in detail in [45]. The experimental setup consists of a conveyor belt and a 1:10 scale model car with mechanically coupled front wheel steering and sprung wheel suspensions (see Fig. 5). The vehicle is attached to the frame of the conveyor belt using a custom 5-degrees-of-freedom suspension system that only constrains the vehicle's motion in the longitudinal direction of the vehicle. The suspension mechanism consists of a roller bearing linear guide with a linear encoder and a custom 3D printed mechanism with ball bearings and magnetic rotary sensors. The sensors in the suspension system provide measurements of the vehicle's lateral position, as well as yaw and roll angles at a high sampling frequency.
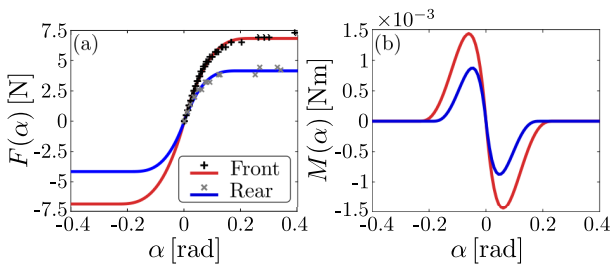
The running conveyor belt provides the relative longitudinal displacement of the road surface with respect to the vehicle, while the steering system is actuated by a servo motor with the steering torque controller (13). The higher-level control algorithm (12) is running on a National Instruments CompactRio 9039 unit, which is also used for data acquisition. The sampling frequency was set to 1 kHz, and an

Table 3
Parameter values of the test rig.

Parameter	Value
Distance between hitch point and front axle (l)	0.22 m
Vehicle wheelbase (f)	0.239 m
Distance between rear axle and center of gravity (d)	0.146 m
Vehicle mass (m)	0.92 kg
Yaw moment of inertia (J_C)	0.018 kgm^2
Steering system moment of inertia (J_F)	4.5·10^{-6} kgm^2
Lower-level steering control proportional gain (k_p)	0.0017 Nm
Lower-level derivative gain (k_d)	1.35·10^{-4} Nms
Longitudinal velocity (V)	8.3 km/h
Time delay (τ)	0.25 s
Linear dissipation in linear guide (b)	0.6 Ns/m
Nonlinear dissipation parameter (ε)	0.02 m/s

Table 4
Tire parameters of the test rig at the front and rear axles.

Parameter	Front axle	Rear axle
Contact patch half-length (a)	0.002 m	0.002 m
Cornering stiffness (C)	84.9 N	65.3 N
Sliding friction coefficient (μ)	1.24	1.18
Rolling friction coefficient (μ_0)	1.24	1.18
Vertical axle load (F_z)	5.5 N	3.5 N
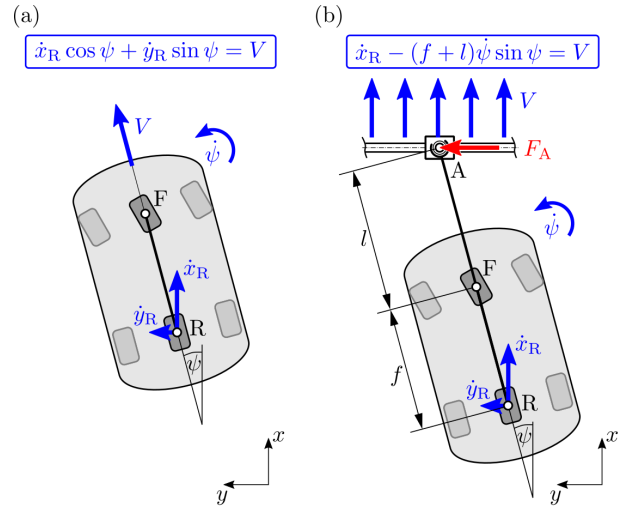
Figure 7: Comparison of (a) a traditional vehicle model and (b) the mechanical model of the experimental setup.

artificial feedback delay was applied in the control unit. For this study, we used the time delay $\tau = 0.25$ s and run the conveyor belt at the speed of $V = 8.3$ km/h in the experiments.

The parameters of the test rig were determined in a series of measurements, and they are collected in Table 3. The tire parameters were identified in a caster-wheel setup, where a constant lateral force was applied to a pair of wheels being towed on the running conveyor belt while measuring the side slip angle. The measurement points (plus signs and crosses) with the fitted brush tire model characteristics (blue and red curves) are shown in Fig. 6 for the front and rear tires. The resulting tire parameters are listed in Table 4.


Figure 6: Tire characteristics of the model vehicle: (a) measured side forces (plus signs and crosses) and the fitted brush tire side force characteristics for the front and rear axles, (b) the self-aligning moment curves of the fitted brush models.

3.2. Modeling of vehicle on conveyor belt

The anchoring of the vehicle in the experimental setup modifies its dynamics compared to the bicycle model detailed in Section 2.1, therefore the measurement results cannot be viewed as direct verification of the analysis of Section 2. In order to account for the differences between the vehicle moving on a road and the vehicle on the conveyor belt, the mechanical model of Section 2 is modified in two ways.

First, the fixed speed V is now generated by the conveyor belt instead of the drivetrain of the vehicle, therefore, the longitudinal speed of the vehicle is not kept constant anymore but it changes depending on the yaw angle ψ (see Fig. 7). Consequently, the kinematic constraint in Eq. (1) needs to be modified so that the global x component of the velocity of the hitch point A is fixed:

$$\dot{x}_R - (f + l)\dot{\psi}\sin\psi = V, \qquad (21)$$

where l denotes the distance between the front axle F and the hitch point A (see Fig. 7). This modified kinematic constraint changes the derivatives of the generalized coordinates to

$$\dot{x}_R = V + (f + l)\sigma_2\sin\psi, \qquad (22)$$
$$\dot{y}_R = \sigma_1\sec\psi + (V + (f + l)\sigma_2\sin\psi)\tan\psi, \qquad (23)$$
$$\dot{\psi} = \sigma_2, \qquad (24)$$
$$\dot{\delta}_s = \sigma_3. \qquad (25)$$

Note that when linearized around the straight-line motion, both Eq. (1) and Eq. (21) leads to $\dot{x}_R = V$, and the kinematics of the two models in Fig. 7 coincide for small vibrations.

The other change compared to the original vehicle model is that we need to consider the additional active force F_A at

the hitch point, see Fig. 7(b). This accounts for the overall dissipation arising in the roller bearing linear guide, including effects such as friction, rolling resistance and viscous damping. To describe the nonlinear characteristic of the dissipation force, which saturates at high speeds, we use the formula

$$F_A = -b\varepsilon \tanh\left(\frac{v_A}{\varepsilon}\right), \quad (26)$$

where v_A denotes the velocity of point A in the y direction, calculated as

$$v_A = \dot{y}_R + (f + l)\dot{\psi}\cos\psi. \quad (27)$$

Note that when linearized, Eq. (26) leads to $F_A = -bv_A$, therefore, parameter b determines the slope of the force characteristic at $v_A = 0$, while ε can be used to adjust the saturation level, i.e., $\sup_{v_A \in \mathbb{R}} F_A = b\varepsilon$. Therefore, in case of small amplitude oscillations, F_A acts as viscous damping, while at higher lateral speeds, it has dry friction-like tendencies. The force characteristic (26) is plotted in Fig. 8. Note that a similar friction force characteristic was reported in e.g. [20] for a linear ball guide. Since the necessary measurement setup was not available to experimentally determine the values of b and ε in the test rig, these parameters were identified indirectly, making sure that the resulting F_A curve remains physically plausible. As listed in Table 3, we used the values of $b = 0.6$ Ns/m and $\varepsilon = 0.02$ m/s, which corresponds to a maximum dissipation force of 0.012 N. Although the magnitude of F_A remains relatively small, it still has a strong effect on the nonlinear dynamics of the system.
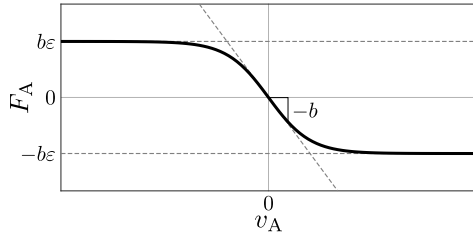
Figure 8: Characteristic of the dissipation force arising in the linear guide.

With the above detailed modifications, the Gibbs–Appell-equations of the vehicle model change to (cf. Eq. (6)-(9)):

$$\begin{bmatrix} m_{11} & m_{12} & 0 \\ m_{21} & m_{22} & J_F \\ 0 & J_F & J_F \end{bmatrix} \begin{bmatrix} \dot{\sigma}_1 \\ \dot{\sigma}_2 \\ \dot{\sigma}_3 \end{bmatrix} = \begin{bmatrix} f_1 \\ f_2 \\ f_3 \end{bmatrix}, \quad (28)$$

with the elements of the generalized mass matrix

$$m_{11} = m\sec^2\psi,$$
$$m_{12} = m_{21} = m((f + l)\tan^2\psi + d), \quad (29)$$
$$m_{22} = J_F + J_C + md^2 + m(f + l)^2\tan^2\psi,$$

and the right hand side

$$\begin{aligned} f_1 = & - F_R - F_F \cos(\psi + \delta_s)\sec\psi + F_A \sec\psi \\ & - mV\sigma_2\sec^3\psi - m\sigma_1\sigma_2\tan\psi\sec^2\psi \\ & - m\sigma_2^2\left((f + l)(1 + \sec^2\psi) - d\right)\tan\psi, \end{aligned}$$

$$\begin{aligned} f_2 = & - M_F - M_R + F_A(f + l)\sec\psi \\ & + F_F\left((f + l)\sin\delta_s\tan\psi - f\cos\delta_s\right) \\ & - mV\sigma_2\left((f + l)\tan^2\psi + d\right)\sec\psi \\ & - m\sigma_1\sigma_2\left((f + l)\tan^2\psi + d\right)\tan\psi \\ & - m\sigma_2^2(f + l)^2\tan\psi\sec^2\psi, \end{aligned} \quad (30)$$

$$f_3 = - M_F + M_s.$$

As in the original vehicle model of Section 2, the tire side forces $F_F(\alpha_F)$ and $F_R(\alpha_R)$ as well as the self-aligning moments $M_F(\alpha_F)$ and $M_R(\alpha_R)$ are determined using the nonlinear brush tire model (see Appendix A). Due to the modified kinematics, however, the calculation of the side slip angles changes to:

$$\alpha_F = \arctan\left(\frac{v_{F,\perp}}{v_{F,\|}}\right), \quad (31)$$

$$\alpha_R = \arctan\left(\frac{\sigma_1\cos\psi}{V + (\sigma_1 + (f + l)\sigma_2)\sin\psi}\right), \quad (32)$$

where the perpendicular ($v_{F,\perp}$) and parallel ($v_{F,\|}$) velocity components of the front wheel are

$$\begin{aligned} v_{F,\perp} = & (\sigma_1 + f\sigma_2)\cos\psi\cos\delta_s \\ & - \left((\sigma_1 + (f + l)\sigma_2)\sin\psi + V\right)\sin\delta_s, \end{aligned} \quad (33)$$

$$\begin{aligned} v_{F,\|} = & (\sigma_1 + f\sigma_2)\cos\psi\sin\delta_s \\ & + \left((\sigma_1 + (f + l)\sigma_2)\sin\psi + V\right)\cos\delta_s, \end{aligned} \quad (34)$$

respectively. Some additional details about the derivation of the equations of motion can be found in Appendix C.2.

3.3. Linear and nonlinear analyses

It was already mentioned previously that the modified kinematic constraint on the test rig does not change the linear dynamics. It might, however, influence the nonlinear behavior of the vehicle, and in addition, the dissipation force F_A appears in the linearized system too. Therefore, this section aims to highlight the differences between the two vehicle models both in terms of linear stability and nonlinear dynamics. The parameter values of the test rig (see Tables 3 and 4) are used for the original and the modified vehicle model as well.

Linearizing the mechanical model of the test rig around $\mathbf{x} = \mathbf{0}$ (where the state vector $\mathbf{x}$ is the same as in Eq. (15)) leads to the state matrix structure

$$\mathbf{A} = \begin{bmatrix} 0 & V & 0 & 1 & 0 & 0 \\ 0 & 0 & 0 & 0 & 1 & 0 \\ 0 & 0 & 0 & 0 & 0 & 1 \\ 0 & A_{42} & A_{43} & A_{44} & A_{45} & A_{46} \\ 0 & A_{52} & A_{53} & A_{54} & A_{55} & A_{56} \\ 0 & A_{62} & A_{63} & A_{64} & A_{65} & A_{66} \end{bmatrix}, \quad (35)$$

while the structure of the input matrix **B** is the same as in Eq. (17). However, the individual matrix elements A_{ij} (listed in Appendix C.2) are now slightly different due to the presence of the dissipation force F_A.
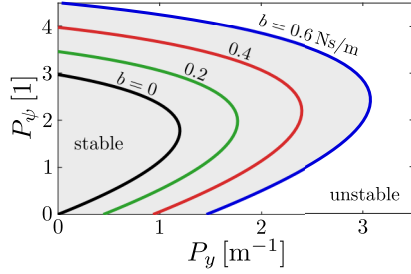

Figure 9: Stable control regions for different values of the dissipation parameter b. Vehicle parameters are listed in Tables 3 and 4.

Figure 9 shows the effect of the dissipation parameter b on the linear stability of the system. It clearly shows that the dissipation in the linear guide has a stabilizing effect, and it can even prevent stability loss for zero (and even some negative) values of the feedback gain P_ψ. The $b = 0$ case means that no dissipation force arises in the linear guide, in which case there is no difference between the two mechanical models in the linear sense, therefore the stability boundaries are also identical.

To compare the nonlinear dynamics of the two vehicle models, we use the same figure structure as in Fig. 4. Figure 10(a)-(c) show bifurcation diagrams at fixed values of the control gain P_ψ. Thin and thick bifurcation branches of limit cycles correspond to the original and modified models, respectively. The bifurcation diagram in Fig. 10(a) is qualitatively very similar to what was observed for real vehicle parameters in Section 2, namely the whole linearly stable domain is bounded by an unstable limit cycle. However, stable limit cycles also emerge at larger amplitudes, through fold points of periodic orbits. In case of the free vehicle model, the stable limit cycle forms a disconnected branch in the bifurcation diagram, since it connects to the lower amplitude branch in the $P_y < 0$ region. We remark that no such disconnected branches were identified for the real vehicle parameter set in the amplitude and control gain region depicted in Fig. 4.

As the value of P_ψ is decreased in panel (b), the fold points where the unstable branches change direction move to larger values of P_y. Consequently, the domain of attraction of the linearly stable straight-line motion is unbounded in some ranges of the control gains. If P_ψ is further decreased, see panel (c), the direction of the branches become almost vertical near the linear stability limit of the original vehicle model, and the limit cycle amplitudes quickly grow to ranges with little practical relevance.

The extended linear stability charts of the two mechanical models are plotted in Fig. 10(d) and (e). The colormap refers to the amplitude y_R^{amp} of the detected unstable limit cycles. In order to concentrate on the physically more relevant, lower amplitude range, the bifurcation diagrams and
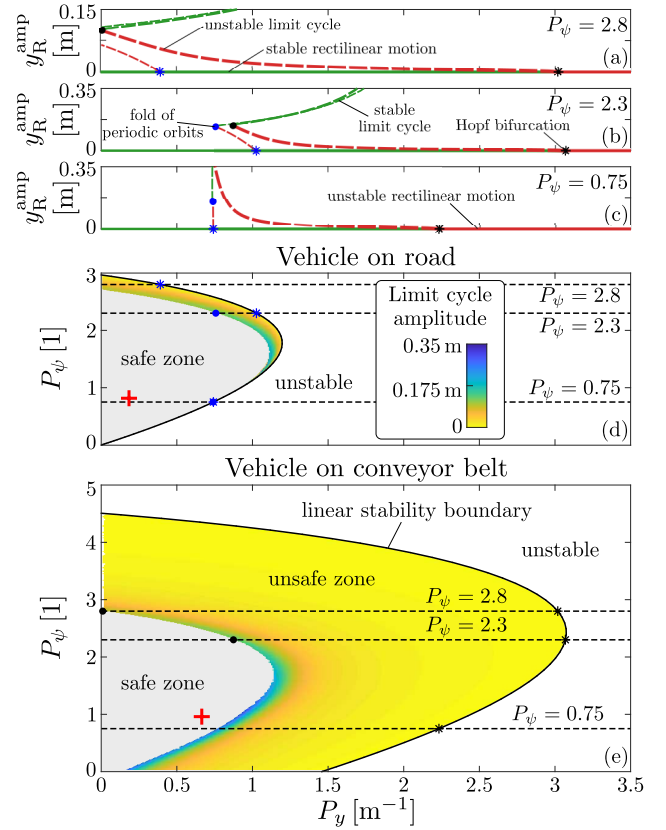
Figure 10: Bifurcation analyses of the original ('on road') and modified ('on the conveyor belt') vehicle models. Panels (a) to (c) show individual bifurcation diagrams along different sections of the stability charts, while the coloring in panels (d) and (e) refers to the amplitudes y_R of the unstable limit cycles in the linearly stable control gain region. Original vehicle model: thin lines and blue symbols in panels (a)-(c), stability chart in panel (d); vehicle model of the test rig: thick lines and black symbols in panels (a)-(c), stability chart in panel (e). Red plus signs denote the optimal control gains of the linear models.

the color coding are limited to a maximum amplitude of 0.35 m. If the unstable limit cycle amplitudes are above this limit (or if the system is globally stable), then the control gains are considered safe against disturbances and the corresponding region of the stable domain is colored in gray. Note that for these specific system parameters, the optimal control gain setup of the linear model (denoted by red plus signs) is inside this safe zone, therefore, if the controller is tuned based only on the dominant poles of the linear model, the nonlinear system will also be sufficiently robust against disturbances.

It is worth mentioning that the additional linearly stable area due to the effect of the dissipation force F_A is enclosed by small amplitude unstable limit cycles. Thus, although dissipation effects in the linear guide make the straight-line motion stable for larger control gains, the domain of attraction of the stable equilibrium is so small in these ranges that the vehicle can very easily lose its stability due to perturbations. This difference between the linear and nonlinear behavior of the test setup could be explained by the saturating
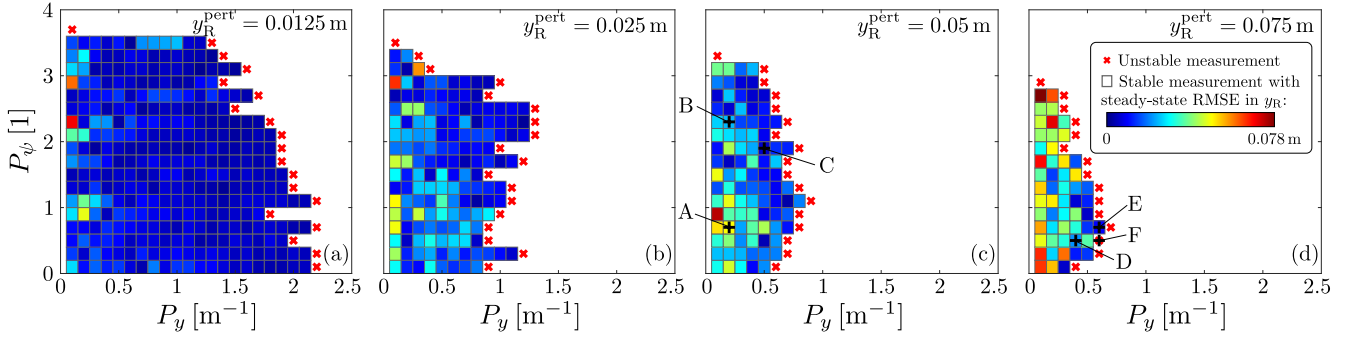
Figure 11: Measurement results for different perturbation levels y_R^{pert}. The coloring of the tiles refers to the root mean square error (RMSE) of the lateral position. Parameter points A to F correspond to the time series shown in Fig. 14.

force characteristic shown in Fig. 8, where the equivalent linear damping is decreased for increasing amplitudes. In the linearly stable control gain domain of the original vehicle model, the limit cycles of the two models start to follow each other relatively closely, indicating similar nonlinear dynamics in both cases.

Overall, even though the linearly stable parameter region is much larger in our experimental setup, the numerical continuation results indicate that the nonlinear behavior of the original system is qualitatively preserved.

3.4. Experimental results

In order to experimentally validate the theoretical results of the nonlinear analysis, the domain of attraction of the straight-line motion of the vehicle was identified using the experimental rig at different control gain setups in the following way. The perturbation of the system was carried out by shifting the reference value of y_R in the controller by the level of y_R^{pert}. If the parallel shift ('lane-change maneuver') could be performed by the controller and the motion of the vehicle tended to the straight-line motion at the new reference value, the perturbation level y_R^{pert} was assumed to be within the domain of attraction of the equilibrium of straight-line motion. If the vibrations of the vehicle did not decay in time (or the vehicle left the conveyor belt), then the perturbation level y_R^{pert} was presumed to be outside the domain of attraction. We swept the parameter domain of interest of the control gains applying four different perturbation levels $y_R^{\text{pert}} \in \{1.25, 2.5, 5, 7.5\}$ cm.

The results of the four measurement series with the different perturbations can be seen in Fig. 11, where colored tiles refer to stable measurements, while red crosses denote the smallest P_y values for which the vehicle lost its stability at a given value of P_ψ. Increasing the perturbation level leads to a decrease in the domain of stabilizing control gains, which agrees with the subcritical behavior that is predicted by the theoretical investigation. Therefore, in order to determine the linear stability limit with experiments, very small perturbations would have to be used to avoid the effect of the unstable limit cycles. However, some physical limitations of the test rig prevent the use of perturbations under a certain

level. Small perturbations generate small desired steering angle values in Eq. (12) and small steering torque in Eq. (13) that might have no effect due to the freeplay and dry friction that occur in the steering mechanism of the model vehicle.

The presence of dry friction and freeplay directly affect the residual error of the controller too, which is illustrated by the color scheme in Fig. 11. The colors correspond to the root mean square error of the controller's lateral error, after cutting the first 20 seconds of the approximately 60 seconds long measurement signals to allow for transients to decay. It can be seen in all four panels that the largest errors occur for small values of P_y. In these cases, even though the vehicle is relatively far from the reference position, the large error signal is multiplied by a small value of P_y, leading to a small desired steering angle, which is unable to show up at the wheels due to dry friction and freeplay. Based on the colors in the upper right area of the stable regions in panels (b) and (c), the best accuracy can be achieved if both P_y and P_ψ is sufficiently large. However, according to panel (d), if the reference path is too far away (the perturbation level is large), such large control gains can already lead to instability.

Figure 12 shows a comparison of the measurement results with the theoretical bifurcation analysis. For each value of P_ψ a measurement series was performed with, the corresponding bifurcation branch is plotted in the panels. Keep in mind that due to the infinite dimensional nature of the system, the limit cycle amplitudes do not exactly correspond to the boundary of the domain of attraction of stable straight-line motion, but they still exhibit qualitatively very similar tendencies. In particular, large values of P_y can ensure stable straight-line motion only for smaller perturbation levels because of the presence of low amplitude unstable limit cycles. Conversely, at lower values of P_y and P_ψ, where no unstable limit cycle is present, the measurements consistently remained stable even for the largest perturbation level. For large values of P_ψ, where the whole linearly stable interval of P_y is enveloped by an unstable limit cycle, increasing the perturbation level can very quickly lead to stability loss.

The comparison between the analytical and measurement results can be seen from another point of view in Fig. 13, where the color of a specific tile in the P_y-P_ψ plane corre-
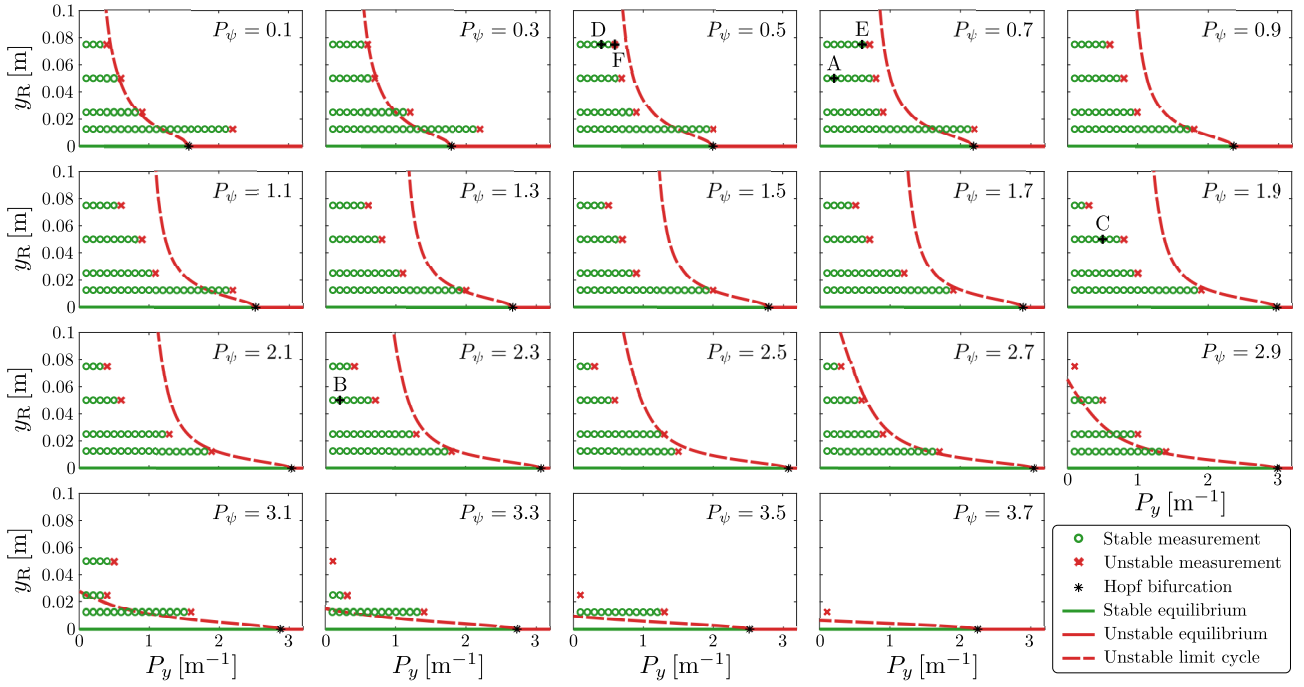
Figure 12: Bifurcation diagrams with measurement results. The theoretical bifurcation branches of the unstable limit cycles are compared to the perturbation levels used in the experiment. Parameter points A to F correspond to the time series shown in Fig. 14.
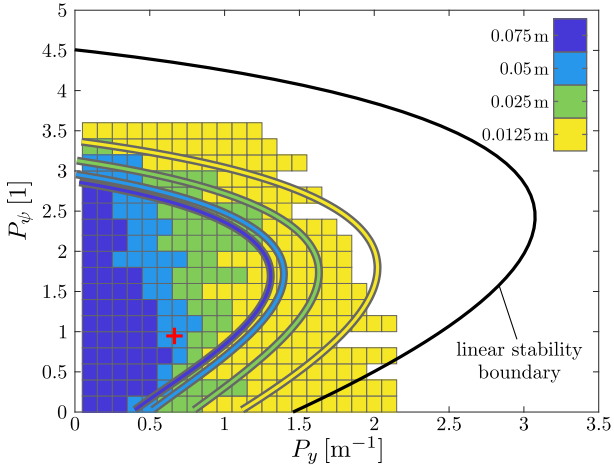

Figure 13: Comparison of limit cycle amplitudes and measurement results. Measurement points are denoted by tiles, where the coloring refers to the largest perturbation that did not push the system out of the stable manifold of straight-line motion. Colored curves show sections of the theoretical unstable limit cycles at the corresponding amplitudes in y_R. Red plus sign denotes the optimal gains suggested by the linear model.

sponds to the maximum perturbation that resulted in a stable measurement with those gains. In addition, sections of the bifurcation diagrams at the corresponding amplitudes are also plotted with similarly colored lines, as well as the analytical linear stability limit in black. Comparing Fig. 13 and Fig. 10, it can be seen that the parts of the linearly stable region where no stable measurement could be performed is

in fact covered by a very small amplitude unstable limit cycle, where possibly even our smallest perturbation pushed the system outside the domain of attraction of the straight-line motion.

For larger perturbations, while at the lower and upper limits of P_ψ good accordance can be observed between the analytical and experimental results, stability loss occurred significantly earlier for middle values of P_ψ than the model would suggest. This difference could possibly indicate some parameter mismatches or that certain nonlinearities are not perfectly accurate in our model. For example, the brush model is one of the more simple nonlinear tire models and the dissipation force characteristic could also be inaccurate. In addition, the domain of attraction of the stable equilibrium depends on the rest of the variables too, while the bifurcation diagrams only show a section of the phase space, which could also explain the differences. Nevertheless, the overall tendencies in terms of nonlinear dynamics are very similar between the mechanical model and the test rig.

We selected some measurement points, marked also in Figs. 11 and 12, to show a few representative time series data from our measurements. In Fig. 14, the evolution of the lateral position of the model car is plotted in these points. The horizontal dashed lines refer to the desired lateral position given by the perturbation levels. The measurement at point A is a typical example where the desired steering angle (due to the small value of P_y) probably remained within the limits of the steering system freeplay, therefore no steering action showed up at the wheels and the vehicle practically remained in its initial position during the whole measurement. A similar scenario can be observed at point B, but in
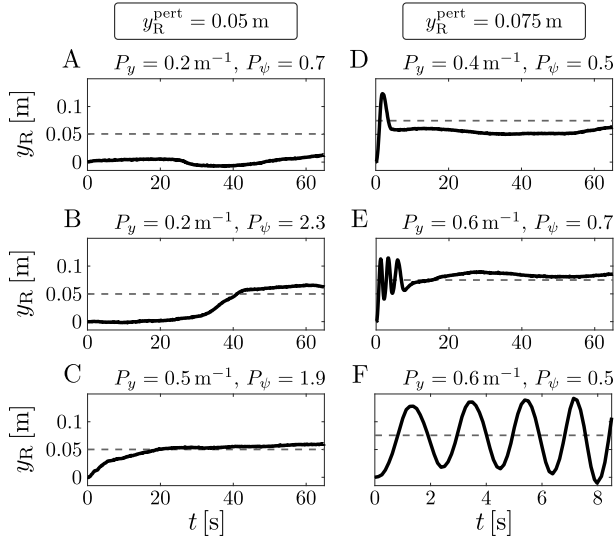
Figure 14: Time series of the rear axle position y_R from a few representative measurements.

this case possibly the measurement noise pushed the steering system over the freeplay limits in the middle of the measurement, and the vehicle eventually performed the lane-change maneuver as intended. The time series at point C shows a smooth but slower settling of the vehicle, while at point D a more dynamic lane change can be seen with some strong overshoot. Point E shows some decaying oscillations near the stability limit, and in point F an oscillatory stability loss can be observed.

We have also checked the frequency components of the measurement signals to compare them to the frequencies predicted by our mathematical models. Distinct peaks in the frequency spectrum could only be identified near the stability boundary, where the vehicle visibly oscillates. At these points, the measured frequencies were mostly in the range of 0.4–1.2 Hz, while the frequencies corresponding to the theoretical linear stability boundary are in the range of 0.25–0.8 Hz. On the one hand, due to the presence of the low amplitude unstable limit cycles, the detected vibrations occurred far from the parameter range of the linear stability boundary. This makes the frequency values hard to compare. On the other hand, it is also not trivial how the measured frequencies could be compared with the theoretical limit cycle time periods. Since the unstable limit cycle is repelling the system, even if we managed to start the measurement from a nearby point of the phase space, the system would only move farther from the limit cycle in time. Thus, instead of measuring the frequency of the unstable periodic motion, the frequency components of some transient dynamics are captured. This can also be seen in the time series of point F in Fig. 14, where the oscillation frequency clearly increases during the measurement.

We remark that due to the anchoring of the vehicle in the experimental setup, the measurement results cannot verifiably prove the existence of the showcased phenomena in real vehicles. However, since the identified unsafe zones are

in good qualitative and quantitative accordance with the theoretical results of the vehicle model on the conveyor belt, it can be assumed that the results of the nonlinear analysis of the vehicle on the road scenario similarly apply in practice.

4. Conclusion

An extensive linear and nonlinear analysis of a lane-keeping controller with time delay was presented in this paper. We showed that including the dynamics of the steering system is an important modeling choice, since it greatly increases the domain of stabilizing control gains compared to the standard bicycle model where the steering angle is directly assigned. The optimal control gains corresponding to the fastest decay of oscillations in the linearized system can also be found in this extended domain of the stable control parameters.

We also showed that relying only on the results of the linear analysis can be misleading: dangerously low-amplitude unstable limit cycles exist around the linearly stable straight-line motion in the stable region of control gains. This means that if the vehicle is sufficiently perturbed to leave the domain of attraction of the stable equilibrium (due to e.g. measurement noise, road surface irregularities, wind gusts, etc.), then it will not be able to converge back to the reference path, and unwanted large amplitude vibrations occur. A safe zone of control gains was identified within the linearly stable region where the unstable limit cycle amplitudes are the largest, therefore the system is the most resilient against disturbances. It was shown that the optimal control gains determined using linear analysis do not necessarily fall into this safe zone, therefore neglecting the nonlinear behavior of the system can introduce significant safety risks.

The strong subcritical behavior suggested by the calculations was successfully reproduced in a series of small-scale laboratory measurements. The bifurcation diagrams created by numerical continuation show good accordance with the experimental results as the domain of control gains stabilizing the vehicle at increasing perturbation levels reduces with similar tendencies.

Overall, both the theoretical and the measurement results indicate a strong sensitivity of the system to disturbances in certain regions of the linearly stable domain of control parameters. This behavior cannot be uncovered by the traditional methods of linear analysis. Therefore, it is even more critical that engineers are aware that such unsafe zones exist within the linearly stable ranges of control gains.

A. Brush tire model

In order to account for the saturation of the tire forces at large side slip angles, the nonlinear brush tire model is used in our analysis. Assuming a parabolic pressure distribution along the contact patch due to the vertical wheel load, the lateral tire forces are calculated as

$$F(\alpha) = \begin{cases} \phi_1 \tan\alpha + \phi_2 \mathrm{sgn}\,\alpha \tan^2\alpha + \phi_3 \tan^3\alpha, & 0 \leq |\alpha| < \alpha_{\mathrm{crit}}, \\ \mu F_z \mathrm{sgn}\,\alpha, & \alpha_{\mathrm{crit}} < |\alpha|, \end{cases}$$

(36)

with coefficients

$$\phi_1 = C,$$

$$\phi_2 = -\frac{C^2}{3\mu_0 F_z}\left(2 - \frac{\mu}{\mu_0}\right),$$

$$\phi_3 = \frac{C^3}{9\mu_0^2 F_z^2}\left(1 - \frac{2\mu}{3\mu_0}\right). \tag{37}$$

The parameters of the brush model include the half-length of the tire-ground contact patch a, the distributed lateral stiffness k, the vertical axle load F_z, as well as the sliding and rolling coefficients of friction μ and μ_0 between the tires and the road. α_{crit} denotes the critical side slip angle where total sliding starts, which is calculated as $\alpha_{\mathrm{crit}} = \arctan\frac{3\mu_0 F_z}{2a^2 k}$ and $C = 2a^2 k$ is the so-called cornering stiffness.

The tire self-aligning moments can also be calculated with the brush tire model, using the formula

$$M(\alpha) = \begin{cases} \mu_1 \tan\alpha + \mu_2\mathrm{sgn}\,\alpha\tan^2\alpha + \mu_3\tan^3\alpha + \mu_4\mathrm{sgn}\,\alpha\tan^4\alpha, \\ \qquad\qquad\qquad\qquad 0 \le |\alpha| < \alpha_{\mathrm{crit}}, \\ 0, \qquad\qquad\qquad\quad \alpha_{\mathrm{crit}} < |\alpha|, \end{cases} \tag{38}$$

where the coefficients are

$$\mu_1 = -\frac{a}{3}\phi_1,$$

$$\mu_2 = -a\phi_2,$$

$$\mu_3 = -3a\phi_3, \tag{39}$$

$$\mu_4 = \frac{aC^4}{27\mu_0^3 F_z^3}\left(\frac{4}{3} - \frac{\mu}{\mu_0}\right).$$

When linearized, the tire side force and self-aligning moment characteristics simplify to $F = C\alpha$ and $M = -\tilde{C}\alpha$ respectively, where $\tilde{C} = \frac{a}{3}C$ is the slope of the self-aligning moment characteristic around zero side slip angle.

B. Saturation function

In order to avoid computational challenges during numerical continuation, the saturation of the desired steering angle in Eq. (13) was implemented as

$$\mathrm{sat}(x) = \begin{cases} x_{\min} & \text{if} \quad x \le x_{\min} - c, \\ x + \frac{(x_{\min} - x + c)^2}{4c} & \text{if} \quad x_{\min} - c < x < x_{\min} + c, \\ x & \text{if} \quad x_{\min} + c \le x \le x_{\max} - c, \\ x - \frac{(x_{\max} - x - c)^2}{4c} & \text{if} \quad x_{\max} - c < x < x_{\max} + c, \\ x_{\max} & \text{if} \quad x \ge x_{\max} + c, \end{cases} \tag{40}$$

where we used $\pm 30°$ as the maximum steering angle and c was set to $5 \cdot 10^{-5}$. The saturation function is plotted in Fig. 15.
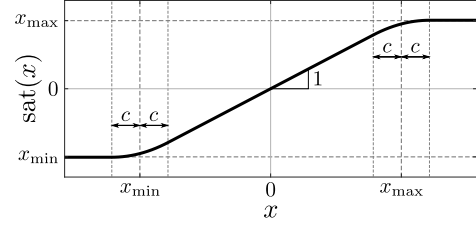
Figure 15: The saturation function used for limiting the desired steering angle.

C. Derivation of the equations of motion
C.1. Vehicle on road

The equations of motion of the vehicle model in Eq. (6) can be derived using the Gibbs–Appell-equations, which are defined as

$$\frac{\partial G}{\partial \dot{\sigma}_i} = \Gamma_i \tag{41}$$

for each pseudo-acceleration $\dot{\sigma}_i$, where G denotes the energy of acceleration (or Gibbs-function) and Γ_i are the so-called pseudo forces. The energy of acceleration of the vehicle model in Section 2.1 is

$$G = \frac{1}{2}J_{\mathrm{F}}(\ddot{\psi} + \ddot{\delta}_{\mathrm{s}})^2 + \frac{1}{2}J_{\mathrm{C}}\ddot{\psi}^2$$
$$+ \frac{1}{2}m(-\ddot{x}_{\mathrm{R}} + d\dot{\psi}^2\cos\psi + d\ddot{\psi}\sin\psi)^2 \tag{42}$$
$$+ \frac{1}{2}m(\ddot{y}_{\mathrm{R}} - d\dot{\psi}^2\sin\psi + d\ddot{\psi}\cos\psi)^2.$$

Substituting the first and second time derivatives of the generalized coordinates based on Eq. (2)-(5), the energy of acceleration can be written as

$$G = \frac{1}{2}J_{\mathrm{F}}(\dot{\sigma}_2 + \dot{\sigma}_3)^2 + \frac{1}{2}J_{\mathrm{C}}\dot{\sigma}_2^2$$
$$+ \frac{1}{2}m(\dot{\sigma}_1 + d\dot{\sigma}_2)^2 + mV\sigma_2(\dot{\sigma}_1 + d\dot{\sigma}_2) + \dots, \tag{43}$$

where terms not depending on the pseudo accelerations are not spelled out. This leads to the partial derivatives

$$\frac{\partial G}{\partial \dot{\sigma}_1} = m(V\sigma_2 + \dot{\sigma}_1 + d\dot{\sigma}_2), \tag{44}$$

$$\frac{\partial G}{\partial \dot{\sigma}_2} = mdV\sigma_2 + md\dot{\sigma}_1 + (J_{\mathrm{F}} + md^2 + J_{\mathrm{C}})\dot{\sigma}_2 + J_{\mathrm{F}}\dot{\sigma}_3, \tag{45}$$

$$\frac{\partial G}{\partial \dot{\sigma}_3} = J_{\mathrm{F}}(\dot{\sigma}_2 + \dot{\sigma}_3). \tag{46}$$

The right-hand side of Eq. (41) can be derived from the virtual power of the active forces:

$$\delta P = \mathbf{F}_{\mathrm{F}}\,\delta\mathbf{v}_{\mathrm{F}} + \mathbf{F}_{\mathrm{R}}\,\delta\mathbf{v}_{\mathrm{R}} - M_{\mathrm{F}}\,\delta(\sigma_2 + \sigma_3)$$
$$- M_{\mathrm{R}}\,\delta\sigma_2 + M_{\mathrm{s}}\,\delta(\sigma_2 + \sigma_3) - M_{\mathrm{s}}\,\delta\sigma_2, \tag{47}$$

where δ refers to virtual quantities and it was taken into account that the steering torque M_{s} acts as an internal torque

between the chassis and the steered wheels. The tire side forces in the vehicle coordinate system (x_1, y_1, z_1) are

$$\mathbf{F}_F = \begin{bmatrix} F_F \sin \delta_s \\ -F_F \cos \delta_s \\ 0 \end{bmatrix}, \quad \mathbf{F}_R = \begin{bmatrix} 0 \\ -F_R \\ 0 \end{bmatrix} \quad (48)$$

and the virtual velocity vectors of points F and R are

$$\delta \mathbf{v}_F = \delta \begin{bmatrix} V \\ \sigma_1 + f\sigma_2 \\ 0 \end{bmatrix}, \quad \delta \mathbf{v}_R = \delta \begin{bmatrix} V \\ \sigma_1 \\ 0 \end{bmatrix}. \quad (49)$$

Substituting the above into Eq. (47), the coefficients of the virtual pseudo-velocities in δP form the pseudo forces:

$$\Gamma_1 = -F_R - F_F \cos \delta_s, \quad (50)$$
$$\Gamma_2 = -M_F - M_R - F_F f \cos \delta_s, \quad (51)$$
$$\Gamma_3 = -M_F + M_s. \quad (52)$$

Equating Eq. (44)-(46) to Eq. (50)-(52) leads to the equations of motion in Eq. (6).

The elements of the state matrix $\mathbf{A}$ of the linearized system in Eq. (16) are the following:

$$A_{43} = \frac{C_F(md(d-f) + J_C) - mdk_p}{mJ_C},$$

$$A_{44} = \frac{(\tilde{C}_R - (C_F + C_R)d + C_F f)dm - (C_F + C_R)J_C}{mVJ_C},$$

$$A_{45} = \frac{C_F f(md(f-d) - J_C)}{mVJ_C} - V,$$

$$A_{46} = -\frac{dk_d}{J_C},$$

$$A_{53} = \frac{C_F(f-d) + k_p}{J_C},$$

$$A_{54} = \frac{(C_F + C_R)d - C_F f - \tilde{C}_R}{VJ_C},$$

$$A_{55} = -\frac{C_F f(f-d)}{VJ_C}, \quad (53)$$

$$A_{56} = \frac{k_d}{J_C},$$

$$A_{63} = \frac{\tilde{C}_F J_C - C_F(f-d)J_F - k_p(J_F + J_C)}{J_F J_C},$$

$$A_{64} = \frac{(\tilde{C}_R - (C_F + C_R)d + C_F f)J_F - \tilde{C}_F J_C}{J_F J_C V},$$

$$A_{65} = \frac{f(C_F J_F(f-d) - \tilde{C}_F J_C)}{J_F J_C V},$$

$$A_{66} = -k_d \frac{J_F + J_C}{J_F J_C}.$$

C.2. Vehicle on conveyor belt

The energy of acceleration of the vehicle model on the test rig can be written in the same form as in Eq. (42), but the first and second time derivatives of the generalized coordinates should be substituted according to Eq. (22)-(25),

which leads to a lengthier expression that we are not including here for the sake of brevity. The partial derivatives of the Gibbs-function are:

$$\frac{\partial G}{\partial \dot{\sigma}_1} = m\dot{\sigma}_1 \sec^2 \psi + m\dot{\sigma}_2((f+l)\tan^2 \psi + d)$$
$$+ mV\sigma_2 \sec^3 \psi + m\sigma_1\sigma_2 \tan \psi \sec^2 \psi \quad (54)$$
$$+ m\sigma_2^2 \left((f+l)(1 + \sec^2 \psi) - d\right) \tan \psi,$$

$$\frac{\partial G}{\partial \dot{\sigma}_2} = m\dot{\sigma}_1((f+l)\tan^2 \psi + d) + (J_F + J_C)\dot{\sigma}_2$$
$$+ m\dot{\sigma}_2((f+l)^2 \tan^2 \psi + d^2) + J_F\dot{\sigma}_3$$
$$+ mV\sigma_2 \left((f+l)\tan^2 \psi + d\right) \sec \psi \quad (55)$$
$$+ m\sigma_1\sigma_2 \left((f+l)\tan^2 \psi + d\right) \tan \psi$$
$$+ m\sigma_2^2(f+l)^2 \tan \psi \sec^2 \psi,$$

$$\frac{\partial G}{\partial \dot{\sigma}_3} = J_F(\dot{\sigma}_2 + \dot{\sigma}_3). \quad (56)$$

The virtual power can be written as

$$\delta P = \mathbf{F}_F \delta \mathbf{v}_F + \mathbf{F}_R \delta \mathbf{v}_R - M_F \delta(\sigma_2 + \sigma_3) - M_R \delta\sigma_2$$
$$+ M_s \delta(\sigma_2 + \sigma_3) - M_s \delta\sigma_2 + F_A \delta v_A, \quad (57)$$

where the only additional term compared to Eq. (47) is the virtual power of the dissipation force. The virtual velocity of point A can be written as

$$\delta v_A = \delta \left((V \sin \psi + \sigma_1 + (f+l)\sigma_2) \sec \psi\right). \quad (58)$$

The rest of the terms in δP are the same as previously, with the exception of the virtual velocity vectors that change to:

$$\delta \mathbf{v}_F = \delta \begin{bmatrix} (V + (\sigma_1 + (f+l)\sigma_2) \sin \psi) \sec \psi \\ \sigma_1 + f\sigma_2 \\ 0 \end{bmatrix}, \quad (59)$$

$$\delta \mathbf{v}_R = \delta \begin{bmatrix} (V + (\sigma_1 + (f+l)\sigma_2) \sin \psi) \sec \psi \\ \sigma_1 \\ 0 \end{bmatrix}. \quad (60)$$

From the virtual power in Eq. (57), the the pseudo forces of the vehicle on the conveyor belt can be calculated as

$$\Gamma_1 = -F_R - F_F \cos(\psi + \delta_s) \sec \psi + F_A \sec \psi, \quad (61)$$

$$\Gamma_2 = -M_F - M_R + F_A(f+l) \sec \psi$$
$$+ F_F \left((f+l) \sin \delta_s \tan \psi - f \cos \delta_s\right), \quad (62)$$

$$\Gamma_3 = -M_F + M_s. \quad (63)$$

After linearizing the equations of the mechanical model

on the test rig, the elements of matrix $\mathbf{A}$ in Eq. (35) are:

$$A_{42} = Vb\left(\frac{d(f-d+l)}{J_C} - \frac{1}{m}\right),$$

$$A_{44} = \big(md\left(\tilde{C}_R - C_R d + C_F(f-d) + b(f-d+l)V\right)$$
$$- (C_F + C_R + bV)J_C\big)/(mVJ_C),$$

$$A_{45} = -\left(C_F f\left(md(d-f) + J_C\right) + V\left(mVJ_C + b(f+l)\right.\right.$$
$$\left.\left.\cdot\left(d(d-f-l)m + J_C\right)\right)\right)/(mVJ_C),$$

$$A_{52} = \frac{Vb(d-f-l)}{J_C},$$

$$A_{54} = \frac{C_R d - \tilde{C}_R + C_F(d-f) + Vb(d-f-l)}{VJ_C}, \qquad (64)$$

$$A_{55} = \frac{C_F f(d-f) + Vb(d-f-l)(f+l)}{VJ_C},$$

$$A_{62} = \frac{bV(f-d+l)}{J_C},$$

$$A_{64} = \big(J_F\left(\tilde{C}_R - C_R d + C_F(f-d) + bV(f-d+l)\right)$$
$$- J_C\tilde{C}_F\big)/(VJ_FJ_C),$$

$$A_{65} = \big(J_F C_F f(f-d) + J_F bV(f+l)(f-d+l)$$
$$- J_C\tilde{C}_F f\big)/(VJ_FJ_C),$$

while elements A_{43}, A_{46}, A_{53}, A_{56}, A_{63} and A_{66} are the same as in Eq. (53).

Acknowledgements

References

[1] Amer, N.H., Zamzuri, H., Hudha, K., Kadir, Z.A., 2017. Modelling and control strategies in path tracking control for autonomous ground vehicles: a review of state of the art and challenges. Journal of intelligent & robotic systems 86, 225–254.

[2] Amidi, O., Thorpe, C.E., 1991. Integrated mobile robot control, in: Mobile Robots V, International Society for Optics and Photonics. pp. 504–523.

[3] Beregi, S., Takács, D., He, C.R., Avedisov, S.S., Orosz, G., 2018. Hierarchical steering control for a front wheel drive automated car. IFAC-PapersOnLine 51, 1–6.

[4] Bloch, A.M., 2003. Nonholonomic mechanics, in: Nonholonomic mechanics and control. Springer, pp. 207–276.

[5] Brennan, S., Alleyne, A., 2002. H-infinity vehicle control using nondimensional perturbation measures, in: Proceedings of the 2002 American Control Conference (IEEE Cat. No. CH37301), IEEE. pp. 2534–2539.

[6] Della Rossa, F., Mastinu, G., 2018a. Analysis of the lateral dynamics of a vehicle and driver model running straight ahead. Nonlinear Dynamics 92, 97–106.

[7] Della Rossa, F., Mastinu, G., 2018b. Straight ahead running of a nonlinear car and driver model–new nonlinear behaviours highlighted. Vehicle system dynamics 56, 753–768.

[8] Della Rossa, F., Mastinu, G., Piccardi, C., 2012. Bifurcation analysis of an automobile model negotiating a curve. Vehicle system dynamics 50, 1539–1562.

[9] Ding, Y., Zhuang, W., Wang, L., Liu, J., Guvenc, L., Li, Z., 2021. Safe and optimal lane-change path planning for automated driving. Proceedings of the Institution of Mechanical Engineers, Part D: Journal of Automobile Engineering 235, 1070–1083.

[10] Dominguez, S., Ali, A., Garcia, G., Martinet, P., 2016. Comparison of lateral controllers for autonomous vehicle: Experimental results, in: 2016 IEEE 19th International Conference on Intelligent Transportation Systems (ITSC), IEEE. pp. 1418–1423.

[11] Engelborghs, K., Luzyanina, T., Roose, D., 2002. Numerical bifurcation analysis of delay differential equations using dde-biftool. ACM Transactions on Mathematical Software (TOMS) 28, 1–21.

[12] Engelborghs, K., Luzyanina, T., Samaey, G., 2001. Dde-biftool v. 2.00: a matlab package for bifurcation analysis of delay differential equations. TW Reports , 61–61.

[13] Fuchshumer, S., Schlacher, K., Rittenschober, T., 2005. Nonlinear vehicle dynamics control-a flatness based approach, in: Proceedings of the 44th IEEE Conference on Decision and Control, IEEE. pp. 6492–6497.

[14] Gao, Y., Gray, A., Carvalho, A., Tseng, H.E., Borrelli, F., 2014. Robust nonlinear predictive control for semiautonomous ground vehicles, in: 2014 American Control Conference, IEEE. pp. 4913–4918.

[15] Gietelink, O., Ploeg, J., De Schutter, B., Verhaegen, M., 2009. Development of a driver information and warning system with vehicle hardware-in-the-loop simulations. Mechatronics 19, 1091–1104.

[16] Greenwood, D.T., 2006. Advanced dynamics. Cambridge University Press.

[17] Heredia, G., Ollero, A., 2007. Stability of autonomous vehicle path tracking with pure delays in the control loop. Advanced Robotics 21, 23–50.

[18] Hoffmann, G.M., Tomlin, C.J., Montemerlo, M., Thrun, S., 2007. Autonomous automobile trajectory tracking for off-road driving: Controller design, experimental validation and racing, in: 2007 American control conference, IEEE. pp. 2296–2301.

[19] Hu, H., Wu, Z., 2000. Stability and hopf bifurcation of four-wheel-steering vehicles involving driver's delay. Nonlinear Dynamics 22, 361–374.

[20] Iwasaki, M., Maeda, Y., Kawafuku, M., Hirai, H., 2006. Precise modeling of rolling friction in ball screw-driven table positioning system. IFAC Proceedings Volumes 39, 295–300.

[21] Kane, T.R., Levinson, D.A., 1985. Dynamics, theory and applications. McGraw Hill.

[22] Kiss, A.K., Avedisov, S.S., Bachrathy, D., Orosz, G., 2019. On the global dynamics of connected vehicle systems. Nonlinear Dynamics 96, 1865–1877.

[23] Kusano, K.D., Gabler, H.C., 2014. Comprehensive target populations for current active safety systems using national crash databases. Traffic injury prevention 15, 753–761.

[24] Kuznetsov, Y.A., 2013. Elements of applied bifurcation theory. volume 112. Springer Science & Business Media.

[25] Liaw, D.C., Chung, W.C., 2008. A feedback linearization design for the control of vehicle's lateral dynamics. Nonlinear Dynamics 52, 313–329.

[26] Liu, Z., Payre, G., 2007. Global bifurcation analysis of a nonlinear road vehicle system. Journal of Computational and Nonlinear Dynamics 2, 308–315.

[27] Liu, Z., Payre, G., Bourassa, P., 2004. Stability and oscillations in a time-delayed vehicle system with driver control. Nonlinear Dynamics 35, 159–173.

[28] Macadam, C.C., 2003. Understanding and modeling the human driver. Vehicle system dynamics 40, 101–134.

[29] Mastinu, G., Biggio, D., Della Rossa, F., Fainello, M., 2020. Straight running stability of automobiles: experiments with a driving simulator. Nonlinear Dynamics , 1–18.

[30] Mobus, R., Zomotor, Z., 2005. Constrained optimal control for lateral vehicle guidance, in: IEEE Proceedings. Intelligent Vehicles Symposium, 2005., IEEE. pp. 429–434.

[31] Olofsson, B., Nielsen, L., 2020. Using crash databases to predict effectiveness of new autonomous vehicle maneuvers for lane-departure

injury reduction. IEEE Transactions on Intelligent Transportation Systems .

[32] Ono, E., Hosoe, S., Tuan, H.D., Doi, S., 1998. Bifurcation in vehicle dynamics and robust front wheel steering control. IEEE transactions on control systems technology 6, 412–420.

[33] Paden, B., Čáp, M., Yong, S.Z., Yershov, D., Frazzoli, E., 2016. A survey of motion planning and control techniques for self-driving urban vehicles. IEEE Transactions on intelligent vehicles 1, 33–55.

[34] Plöchl, M., Edelmann, J., 2007. Driver models in automobile dynamics application. Vehicle System Dynamics 45, 699–741.

[35] Ren, D., Zhang, J., Zhang, J., Cui, S., 2011. Trajectory planning and yaw rate tracking control for lane changing of intelligent vehicle on curved road. Science China Technological Sciences 54, 630–642.

[36] Rossetter, E.J., Gerdes, J.C., 2005. Lyapunov based performance guarantees for the potential field lane-keeping assistance system. Journal of Dynamic Systems, Measurement, and Control 128, 510–522.

[37] Shen, S., Wang, J., Shi, P., Premier, G., 2007. Nonlinear dynamics and stability analysis of vehicle plane motions. Vehicle System Dynamics 45, 15–35.

[38] Sieber, J., Engelborghs, K., Luzyanina, T., Samaey, G., Roose, D., 2014. Dde-biftool manual-bifurcation analysis of delay differential equations. arXiv preprint arXiv:1406.7144 .

[39] Sternlund, S., Strandroth, J., Rizzi, M., Lie, A., Tingvall, C., 2017. The effectiveness of lane departure warning systems—a reduction in real-world passenger car injury crashes. Traffic injury prevention 18, 225–229.

[40] Strogatz, S.H., 2018. Nonlinear dynamics and chaos with student solutions manual: With applications to physics, biology, chemistry, and engineering. CRC press.

[41] Tagne, G., Talj, R., Charara, A., 2013. Higher-order sliding mode control for lateral dynamics of autonomous vehicles, with experimental validation, in: 2013 IEEE Intelligent Vehicles Symposium (IV), IEEE. pp. 678–683.

[42] True, H., 1999. On the theory of nonlinear dynamics and its applications in vehicle systems dynamics. Vehicle System Dynamics 31, 393–421.

[43] Várszegi, B., Takács, D., Orosz, G., 2019. On the nonlinear dynamics of automated vehicles–a nonholonomic approach. European Journal of Mechanics-A/Solids 74, 371–380.

[44] Vörös, I., Takács, D., 2020. Bifurcation analysis of a lane keeping controller with feedback delay, in: ASME 2020 International Design Engineering Technical Conferences and Computers and Information in Engineering Conference, American Society of Mechanical Engineers Digital Collection.

[45] Vörös, I., Turányi, L., Várszegi, B., Takács, D., 2021. Small-scale experimental test rig for lateral vehicle control. Periodica Polytechnica Mechanical Engineering 65, 163–170.

[46] Vörös, I., Várszegi, B., Takács, D., 2020. The effects of tire dynamics on the performance of finite spectrum assignment of vehicle motion control. Journal of Vibration and Control , 1077546320971161.

[47] Weir, D.H., McRuer, D.T., 1970. Dynamics of driver vehicle steering control. Automatica 6, 87–98.

[48] Werling, M., 2011. Ein neues Konzept für die Trajektoriengenerierung und-stabilisierung in zeitkritischen Verkehrsszenarien. volume 34. KIT Scientific Publishing.

[49] Werling, M., Gröll, L., Bretthauer, G., 2010. Invariant trajectory tracking with a full-size autonomous road vehicle. IEEE Transactions on Robotics 26, 758–765.

[50] Zhang, H., Wang, J., 2015. Vehicle lateral dynamics control through afs/dyc and robust gain-scheduling approach. IEEE Transactions on Vehicular Technology 65, 489–494.

[51] Zhao, P., Chen, J., Song, Y., Tao, X., Xu, T., Mei, T., 2012. Design of a control system for an autonomous vehicle based on adaptive-pid. International Journal of Advanced Robotic Systems 9, 44.